Composites Science and Technology 167 (2018) 251–259

Contents lists available at ScienceDirect

Composites Science and Technology

journal homepage: www.elsevier.com/locate/compscitech

Enhanced fracture toughness in architected interpenetrating phase composites by 3D printing

Tiantian Li**, Yanyu Chen, Lifeng Wang*

Department of Mechanical Engineering, State University of New York at Stony Brook, Stony Brook, New York, 11794, USA

ARTICLE INFO

Keywords:
Architected materials
Interpenetrating phase composites
Fracture toughness
3D printing
Multifunctional

ABSTRACT

Interpenetrating phase composite (IPC), also known as co-continuous composite, is one type of material that may exhibit an unusual combination of high stiffness, strength, energy absorption, and damage tolerance. Here we experimentally demonstrate that IPCs fabricated by 3D printing technique with rationally designed architectures can exhibit a fracture toughness 16 times higher than that of conventionally structured composites. The toughening mechanisms arise from the crack-bridging, process zone formation and crack-deflection, which are intrinsically controlled by the rationally designed interpenetrating architectures. We further show that the prominently enhanced fracture toughness in the architected IPCs can be tuned by tailoring the stiffness contrasts between the two compositions. The findings presented here not only quantify the fracture behavior of complex architected IPCs but also demonstrate the potential to achieve tailorable mechanical properties through the integrative rational design and the state-of-the-art advanced manufacturing technique.

1. Introduction

Structural systems in the defense, aerospace, automotive, energy, and semiconductor industries are often subjected to complex loading conditions, such as multi-axial loading, vibration, shock, and high-velocity impact. This triggers the demands for the development of innovative structural materials, possessing a compelling combination of mechanical robustness, lightweight, affordability, and versatility. Composite materials consisting of multiple compositions can have improved overall performance due to the synergistic contribution of each composition in the composites. Among these composites, interpenetrating phase composite (IPC, also known as co-continuous composite), in which each constituent phase forms a completely interconnected three-dimensional (3D) network, has attracted a lot of research interests [1–4]. Indeed, the interpenetrating microstructures are widely spread in biological structural materials, such as sea urchin skeleton [5], human bone [6], microvascular networks [7], and botanical systems [8]. These natural IPCs exhibit rich multifunctionalities including thermal, mechanical, and other transport properties. Intrinsically, these prominent properties are controlled by their inherent architectures. Each constituent phase completely interpenetrates through the composite microstructure in all three dimensions and contributes the maximum of its most desirable properties to the overall properties of the composite, thereby endowing the composite with a more attractive combination of properties and functionalities.

To understand the multifunctionalities observed in the natural IPC systems, considerable efforts have been recently devoted to developing analytical models and computational frameworks to evaluate the effective thermal and mechanical performance of synthesized IPCs. For example, analytical methods based on Voigt and Reuss models can accurately predict the effective thermal and mechanical properties of the IPC [8–11]. Numerical methods such as finite element analyses have been extensively employed to capture the elastic, thermal, dynamic, and fracture properties of IPCs [12–23]. It should be pointed out that most of these IPCs are fabricated using conventional methods, such as squeeze casting process and pressureless melt infiltration [24,25], where each phase of these IPCs is randomly distributed. Though the volume fraction can be precisely controlled, the inherent architecture is still ill-defined. For example, the dimensions of the ligaments have a nonuniform feature and each composition is randomly dispersed, which poses a great challenge to fabricate IPCs with fewer defects and accurately predict their effective properties.

Recently, studies show that materials with well-defined architectures could be exploited to explore new properties and novel functionalities [26–30]. Computational design methods, such as topology optimization algorithms, have been developed to define the ideal

---

* Corresponding author.
** Corresponding author.
E-mail addresses: tiantian.li.1@stonybrook.edu (T. Li), Lifeng.wang@stonybrook.edu (L. Wang).

https://doi.org/10.1016/j.compscitech.2018.08.009
Received 26 March 2018; Received in revised form 22 June 2018; Accepted 9 August 2018
Available online 11 August 2018

arrangement of composites with two or more materials to achieve optimum macroscopic properties [31], mostly focusing on the mechanical [32–34], electrical [35] and thermal properties [36]. Along with these, advanced additive manufacturing techniques, such as 3D printing, have gained much attention due to its capability of creating complex topologies with fine features composed of a multitude of materials with varying mechanical properties quickly, cheaply, and at a large scale [37–41]. For example, improved impact resistance has been observed in 3D printed bioinspired composites with hierarchical conch shell structures, indicating a crack-arresting mechanism embedded in the natural architecture [42]. As reported in our previous work, the 3D periodic IPCs based on the triply periodic minimal surfaces (TPMS) of glassy polymer/rubbery polymer materials at micrometer resolutions can be readily fabricated through 3D printing [22]. A combination of high stiffness, strength, energy absorption, and damage tolerance have been achieved in the 3D printed IPCs with different lattice symmetries. More recently, more TPMS topologies are used to design IPCs and their compressive properties and electrical conductivities [43] are experimentally tested [44–46] and numerically analyzed [43,45]. However, a quantitative understanding of the fracture behavior of architected IPCs is still lacking and especially the measurement of the fracture toughness of such complex materials is less well defined.

In this paper, we investigate the fracture toughness of a group of 3D printed IPCs with different lattice symmetries. Three-point bending tests are performed on the singled edge notch bend (SENB) samples to quantify the fracture properties. The results are compared with conventionally architected composites with particle reinforced, fiber reinforced, and laminates topologies. Furthermore, we demonstrate that the fracture toughness of the proposed IPCs can be tuned through controlling the stiffness contrast and volume fraction of the compositions.

2. Materials and methods

2.1. Architected IPCs

The model system of the IPCs studied here is based on microstructures which combine the rod-connected lattices and their inverse counterparts. Here three lattice symmetries are considered including simple-cubic (SC), body-centered-cubic (BCC), and face-centered-cubic (FCC) lattices. Fig. 1(a–c) displays the proposed 3D periodic SC, BCC, and FCC IPCs where the volume fraction of each phase is set to 50%. In our design, the phase of rod-connected lattices is set as the hard domain and the inversed phase is set as the soft domain. Compared to previous IPCs with triply periodic minimal surfaces [22], these IPCs with rod-connected counterparts are easier for design with simple geometric parameters and unit cells. The symmetry and volume distribution in these structures can be precisely controlled by tailoring the radius of rod ligaments. The relations between the volume fraction of rod-connected lattices' domain, $\bar{\rho}$ and the radius/periodicity ratio, r/l are given by:

$$\bar{\rho} = 3\pi\left(\frac{r}{l}\right)^2 - C_1\left(\frac{r}{l}\right)^3 \text{ for SC,} \tag{1}$$

$$\bar{\rho} = 4\sqrt{3}\pi\left(\frac{r}{l}\right)^2 - C_2\left(\frac{r}{l}\right)^3 \text{ for BCC,} \tag{2}$$

$$\bar{\rho} = 12\sqrt{2}\pi\left(\frac{r}{l}\right)^2 - C_3\left(\frac{r}{l}\right)^3 \text{ for FCC,} \tag{3}$$

where the radius of the rod ligaments is r and the length of the unit cell is l. The cubic correction coefficients $C_1 = 11.318$, $C_2 = 39.201$ and $C_3 = 154.518$ have been identified from fitting Eqs. (1)–(3) to CAD calculations [47].

In addition to the IPCs, the particle-reinforced composites (PCs), the fiber-reinforced composites (FCs) and the laminal-reinforced composites (LCs) are also designed and fabricated with the same amount of compositions to compare the fracture toughness.

2.2. Sample fabrication

The specimens are fabricated using a multi-material 3D printer (Objet Connex 260, Stratasys) and multiple photocurable prepolymers are used to form the hard and soft components. In this work, VeroWhitePlus, a glassy polymer, is used for the hard domains (labeled "*A*") and TangoPlus, which is highly rubbery, is used for the soft domains (labeled "*B*"). The stiffness contrast between these two phases can be tailored by mixing VeroWhitePlus and TangoPlus via a digital material mode in the printer. The mixed materials are used for the soft component (labeled as "*B*1", "*B*2", "*B*3", "*B*4" and "*B*5"). The specimens for the fracture toughness measurement are shown in Fig. 1(d), which consist of 54 × 12 × 6 unit cells, resulting in a dimension of 135 mm × 30 mm × 15 mm. The minimum geometric size of inner structures in the composites is around 200 μm, which is at least one order of magnitude greater than the minimum resolution (16 μm) provided by the 3D printer. Considering the anisotropic nature of 3D printing, the layer orientation is found to influence the mechanical properties of the material; therefore, all the specimens are printed along the same orientation. The as-fabricated specimens are kept at room temperature for 7 days to allow for the saturation of the curing. (See Supplementary Information for more details).

2.3. Mechanical testing

The uniaxial tensile tests for the constitutive materials and uniaxial compression tests for IPC specimens are performed using the same MTS mechanical tester (C43 frame). All the experiments are conducted in a quasi-static regime with a constant strain rate of 0.001 s^{-1}. The load-displacement curves measured from the uniaxial compression tests are then transferred into nominal stress-strain behaviors based on the measured dimensions of the specimens. Young's modulus E_{XX} and yield stress σ_{XX} for each specimen are calculated from the nominal stress-strain curves. For fracture toughness measurement, three-point bending tests are performed with the same mechanical tester at a constant displacement rate of 0.5 mm/min. Images of the specimens at various loading conditions are taken at a rate of 0.08 FPS. (See Supplementary Information for more details).

2.4. Calculation of fracture toughness

The fracture toughness is determined using a singled edge notch bend (SENB) sample following the procedure outlined in ASTM standard E1820 (ASTM E1820, 2013), as shown in Fig. 1(d)-(f). This method is designed to determine the fracture toughness of metallic materials which are pure homogeneous. While with the rapid developing of modern material manufacturing, many new materials such as composites and cellular materials have been designed and fabricated. Recently, this method has been applied to study the fracture toughness of these new materials with non-homogeneous structures or phases [48–50]. Moreover, our previous study shows that 3D periodic IPCs of glassy polymer/rubbery polymer materials tend to be isotropic on the macroscopic scale and their mechanical behavior is often similar to homogeneous materials [22]. Therefore, this method based on ASTM 1820 is well-suited for detecting and calculating the fracture behavior for the 3D printed periodic IPCs. The combination of starter notch and fatigue pre-crack shall conform to the ASTM standard requirements shown in Fig. 1(e). A very sharp notch tip with the angle of 30° is designed to promote early crack initiation. The *J*-approach is employed to capture inelastic contributions to the fracture resistance using the elastic compliance method in ASTM E1820. Compliance measurements from the unloading curves are made at intervals $\Delta v = 0.25$, 1 and 1 mm for the SC, BCC and FCC IPC samples, respectively. Calculation of the

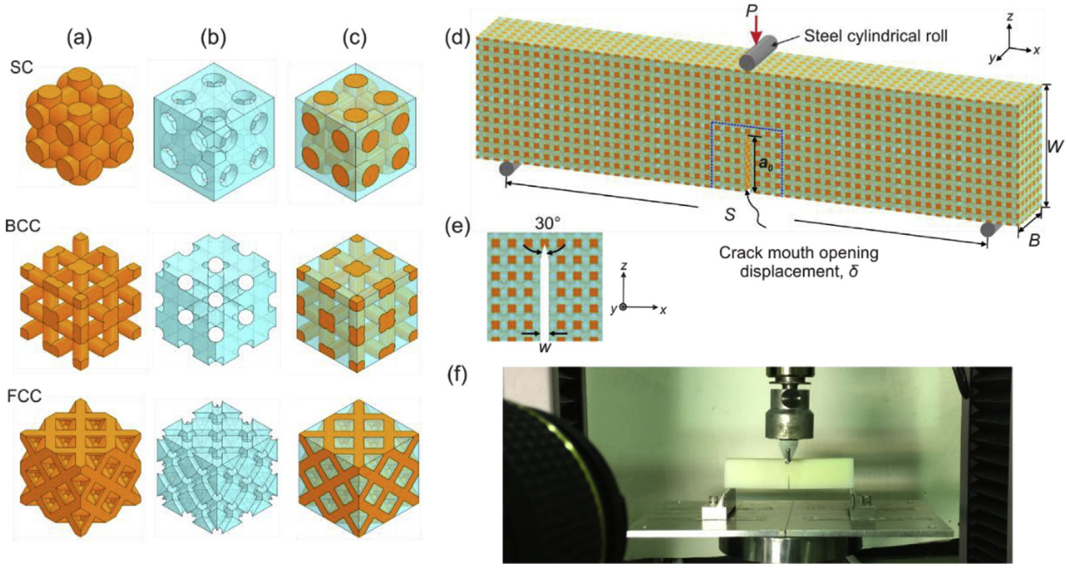

Fig. 1. Schematics of 3D IPCs with different lattice symmetries. (a) 3D periodic IPCs consisting of 2 × 2 × 2 representative volume elements with simple cubic, body-centered-cubic, and face-centered-cubic lattice symmetries. (b) The corresponding phase of a rod-connected counterpart in each IPC. (c) The corresponding inverse phase in each IPC. Experimental setup for the 3-point bending test. (d) Single edge notched bend (SENB) specimen and test configuration. The dimensions of the specimen are defined as the width W, the length L and the thickness B. The load P is applied in the mid of specimens and the span length is S. The initial length of the notch is defined as a_0. (e) The crack starter notch, where the width of the notch is defined as w and the angle of the initial crack tip is 30°. (f) The experiment setup of 3-point bending test of SENB specimen.

current crack length uses the compliance along the loading line, and the J-approach is calculated using the measured applied load and crack mouth opening displacement, δ. The fracture toughness, $K_{J\,(i)}$, is related to the J-approach by $K_{J\,(i)} = (J_{(i)}E')^{1/2}$, where E' is the plane strain Young's modulus, $E' = E_S/(1-\nu^2)$ and ν is the Poisson's ratio. Since the samples were composites and not homogeneous solid materials, this study used the measured compressive moduli along the span length, E_{XX}. (See Supplementary Information for more details).

3. Results and discussion

3.1. Fracture behavior of IPCs

Before systematically examining the fracture behaviors of proposed IPCs, the fracture response of the two base materials used for 3D printing the composite, material *A*, and material *B* is first investigated (Fig. 2(a)). The load-displacement curves obtained from the three-point bending test of SENB samples clearly show the significant distinction between the constitutive behaviors of these two materials. From the compression tests we have performed on the 3D printed materials, the results show that the stiffness of material *A* is three orders of magnitude higher than the stiffness of material *B*, by a factor of ≈1350. Therefore, the more compliant base material *B* fails at an order of magnitude higher displacement than its less compliant counterpart *A*. Moreover, both samples fail in a brittle manner immediately upon crack propagation.

Fig. 2(b) plots the load, P, as a function of load-line displacement, v, for three lattices, SC, BCC, and FCC IPCs. The load-displacement curves for IPCs exhibit initial linear elasticity, non-linear plasticity before the maximum load and the drops in load which are related to the failure of structures. Compared with the fracture behavior of each composition, the IPCs samples show a highly nonlinear behavior. The continuous soft material phase distributes stress and strain effectively throughout the sample, inducing an additional support to generate more plastic deformation instead of the brittleness of the hard material. Therefore, the extrinsic and intrinsic toughening mechanisms of 3D periodic IPCs from inhibiting damage mechanisms include stretching of the hard polymer that bridges the advancing crack and is also associated with plasticity. As a result, it is effective against the initiation and propagation of cracks. Fig. 2(c-e) presents the in-situ images of the deformed configuration of each IPC at different displacements. Before the first peak load, the large deformation of the material around the precrack tip is visible on the surface of each IPC. After the first peak load, the fracture propagation could be observed. The drops in load after the maximum peak are not continuous but have several steps. This is because the inherent architectures of IPCs play a significant role in preventing the propagation of cracks continuously. Based on the energy principles, the crack will choose the path of the least resistance such as in the soft material. However, the structures of 3D periodic IPCs contain continuous hard and soft materials with multiple constrains which will inhibit the crack propagation in only one phase. Furthermore, FCC IPC exhibits smaller load dropping steps due to the more complexity of microstructures compared with SC and BCC IPCs. For the SC IPC, the images clearly portray that the crack path eccentrically is upon the initial crack tip. Similarly, in the BCC and FCC IPCs, evidently the fracture path has the zigzag shape and the lateral surfaces of the crack are very rough. This phenomenon can be explained based on the energy principle that the crack path will result in a trade-off between the minimum crack deflection angle and the path of least stiffness. Moreover, it's observed that the interfacial adhesion of the 3D printed constituent materials is so strong that the composites do not fail at the interfaces. The proposed IPCs exhibit impressive mechanical characteristics activated by the rationally designed interpenetrating architecture.

To further understand the fracture behavior of the proposed IPCs, Digital Image Correlation (DIC) measurement system is used to quantitatively understand the deformation and crack propagation of these specimens. Fig. 3(a) shows the measured force-displacement relation of three-point bending test and the images in Fig. 3(b) and (c) exhibit the horizontal strain contours related to the main deformation of the IPC-BCC and IPC-FCC respectively which also reflect the stress distributions during the whole loading process. Notice that in the elastic loading stage, the strain distributes mostly behind the crack tip (b1 and c1). Prior to tip failure, as shown in b2, c2, and c3, the strain concentrates ahead of the crack tip to inhibit damage mechanisms, such as cracking which will toughen the IPCs. After tip failure, clearly, the fracture

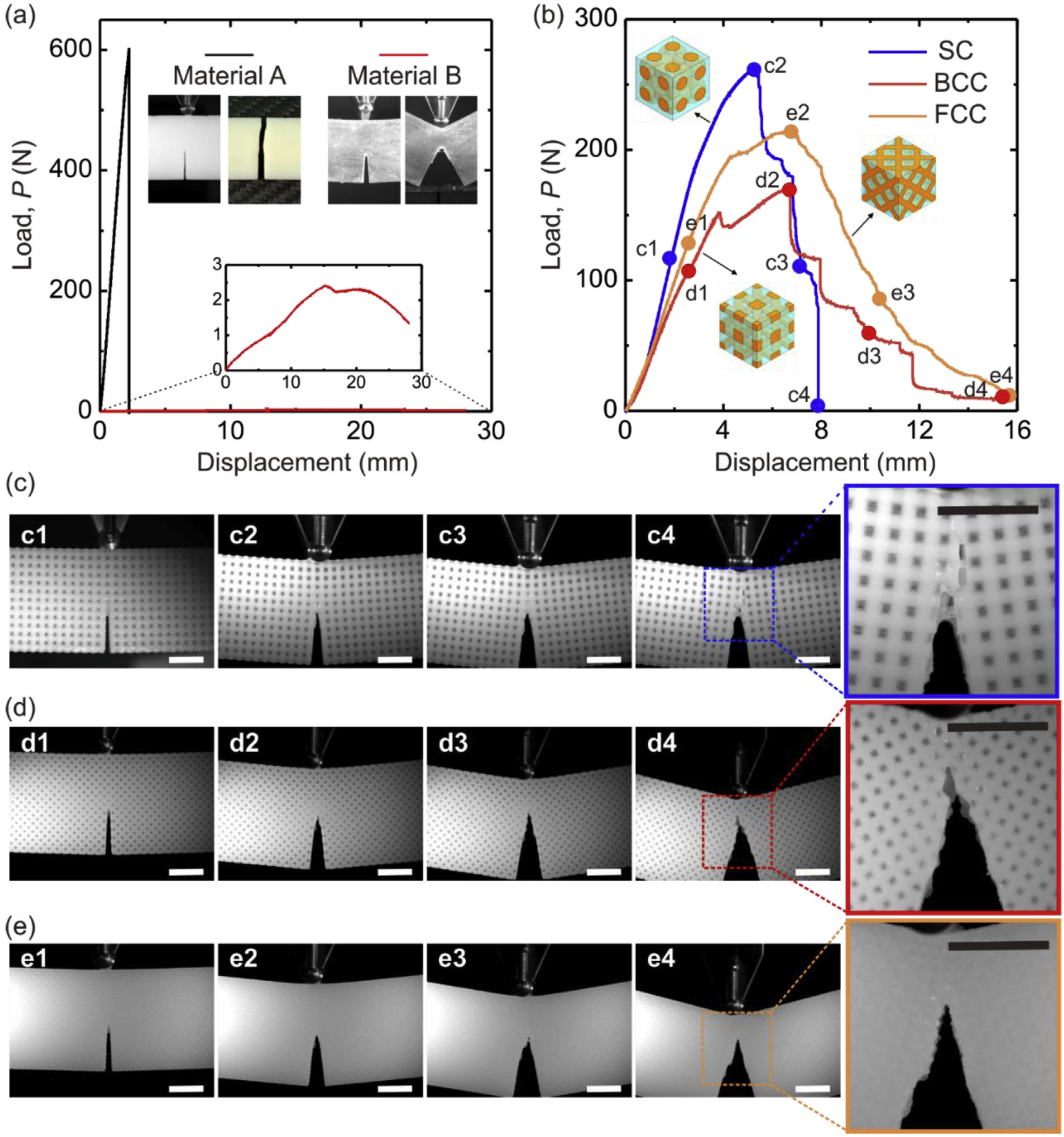

Fig. 2. 3-point bending tests of the SENB specimens. (a) Load-displacement curves of material *A* and material *B*. (b) Load-displacement curves of IPCs with SC, BCC and FCC lattice symmetries. (c)–(e) Images of test specimens at various loading displacements which are marked in the load-displacement curves. Scale bar: 1 cm.

appears in several positions where the strain distributes around as shown in b3-b6. A similar phenomenon could be visualized in c4-c6. With crack propagating, the strain concentration delocalizes to different directions and form longer crack path as shown in b7-b8 and c7-c8, which will extend the load-displacement curves in Fig. 3 (a). Therefore, these images clearly portray that the 3D printed IPCs exhibits impressive mechanical characteristics in terms of fracture propagation. The periodic IPC structures toughen the composites with improving the plasticity of the hard material. Moreover, the soft material delocalizes the stress concentration, enabling the crack propagates in a stable fashion through the system and allowing the sample to sustain increased deformation and significant loading throughout large portions of the fracture process. Furthermore, the periodic interpenetrating phases diverge and extend the crack path which will improve the fracture toughness of the IPCs.

It's demonstrated that both intrinsic toughening mechanism (enlarging of plastic deformation of hard polymer) and extrinsic toughening mechanism (crack deflection, process zone formation and bridging controlled by hard polymer) are synergistically responsible for the enhanced fracture behavior of the proposed IPC composites. Typically, the extrinsic toughness mechanism is effective in resisting crack propagation and is strongly dependent on the crack size. As a result, instead of a constant fracture toughness, the crack-propagation resistance curve (*R*-curve) exhibits a gradually increasing behavior as the crack advances. To further understand these two different mechanisms, the materials *R*-curves for the proposed IPC composites are measured. As shown in Fig. 4, all of the IPC composites with SC, BCC, and FCC lattice symmetries exhibit an increased *J*-integral as the cracks propagate. The absolute value of J-integral in FCC composite is the largest while the SC composite shows the lowest *J*-integral. Noticeably, when converting the

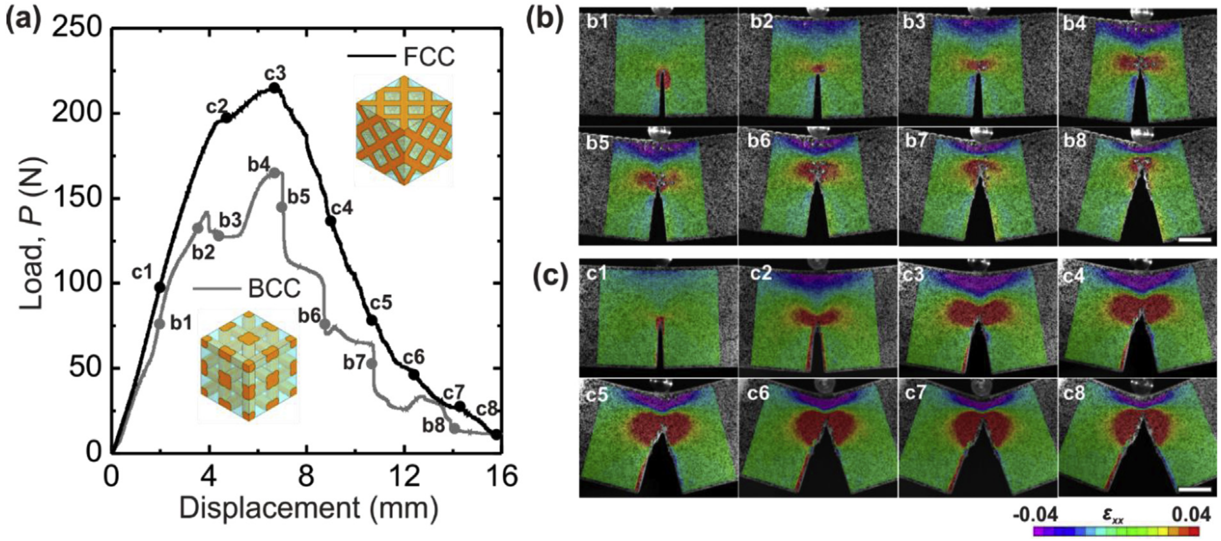

Fig. 3. 3-point bending tests of the SENB specimens of IPC-BCC and IPC-FCC. (a) load-displacement curve. Experimental strain contours of (b) IPC-BCC and (c) IPC-FCC using digital image correlation at various loading displacements which are marked in the load-displacement curves. Scale bars are both 1 cm.

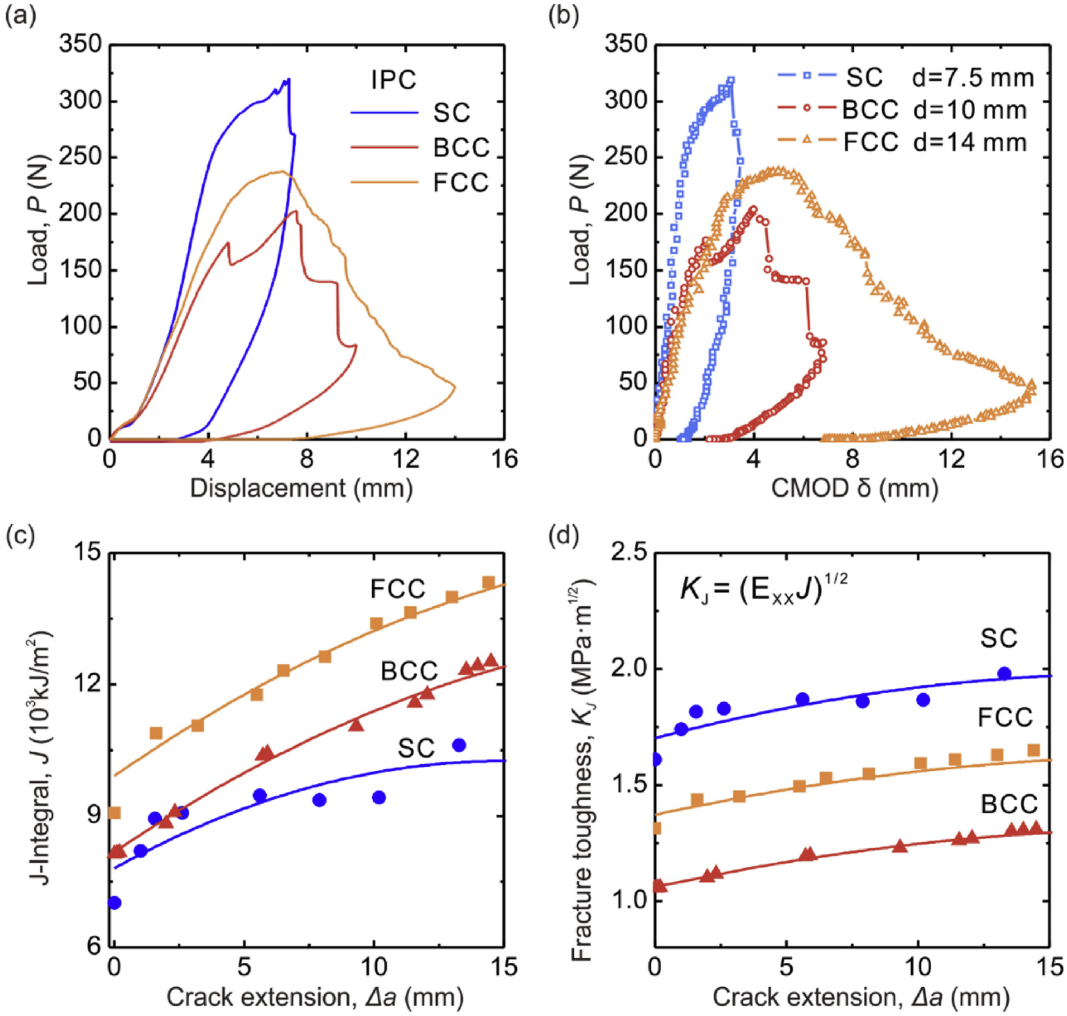

Fig. 4. Representative responses of IPC SENB samples with SC, BCC and FCC lattice symmetries showing the load as a function of (a) the load line displacement, and (b) the crack mouth opening displacement, δ. The crack-growth (c) J-integral, J_{IC} and (d) fracture toughness, K_{JIC} are plotted as a function of crack extension, Δa for IPC SENB samples, respectively. Lines through the data were added to aid the reader.

J-integral into equivalent fracture toughness, SC composite exhibits the largest fracture toughness while FCC composite exhibit an intermediate absolute value. Yet, a gradually increasing toughness still persists in the all of these composites as the cracks propagate. Three major toughening mechanisms are synergistically responsible for the enhanced fracture behavior of the proposed IPCs. The first is the development of a crack bridging zone, in which the hard material phase stretches between the faces of the crack for some distance behind the crack tip. It is clearly seen in Fig. 2(c) that these bridging ligaments begins to stretch immediately behind the crack tip and continue to stretch as the crack advances until they reach a rupture strain, at which point they break. The energy dissipated by these stretching ligament as the crack tip advances by a unit increment gives the increase in the *J*-integral associated with bridging. The second toughening mechanism for the rising *R* curve is the process zone formation ahead and behind the crack tip. The strain contours of the IPCs during crack propagation (Fig. 3(b) and (c)) exhibit that the process zone with large Mises stresses and secondary cracking forms quickly and grows significantly. The formation of process zone is because of the enlarging of plastic deformation of hard material phase from soft material phase's additional support. As the crack grows, the crack tip passes through this zone and materials behind the crack tips begin to unload elastically from a state of plasticity. Upon unloading, the dissipated energy contributes to the toughness of the material. Moreover, the increasing process zone will result in an increasing fracture toughness during the crack propagation. The third toughening mechanism accounting for the rising *R* curve is the crack deflection. Fig. 2 (c)-(e) clearly show that the crack path eccentrics the initial crack tip and continues with a zig-zag shape. The crack deflection increases the area of the fracture surface which elevates the toughness. Above all, the importance of the interpenetrating phase morphology in IPCs show advantages in the resistance of crack propagation. Though it has been extensively demonstrated that natural structural materials such as hierarchical nacreous composites exhibit both intrinsic and extrinsic toughening mechanisms [51,52], similar toughening mechanism are achievable in rationally designed and 3D printed architected composites.

Since IPCs exhibit impressive fracture behavior due to the inherent microstructures, the fracture response of IPCs is compared with several conventional composites, including particle-reinforced, fiber-reinforced, laminal-reinforced topologies. Here, 50% volume fraction of hard material for each design is used for the purposes of fair comparison. For IPCs and PCs, three lattice topologies as SC, BCC, and FCC are selected. For FCs and LCs, two topologies with fiber or laminal as 0° and 90° are selected. The specific composite topology has a significant impact on the overall mechanical response of the SENB samples under three-point bending test. From the load-displacement curves (Fig. 5(a)), the conventional PCs, FCs and LCs exhibit relatively poor mechanical behaviors compared with IPCs. This is because, in conventional composites, the matrix is soft material while the phase of the hard material is not continuous. During the fracture propagating, the crack will choose the path of least resistance which is the continuous compliant matrix. In Fig. 5(b), the crack propagates along the soft material in conventional composites. By contrast, the structures of 3D periodic IPCs contain continuous hard and soft materials with multiple constrains which will inhibit the crack propagation in only one phase. The fracture toughness, K_{JIC} at the crack initiation of each composite calculated based on Equation (S9), is plotted in Fig. 5(b). Here, we demonstrate that the detection and measurement of cracks, particularly in the early stages of a specimen's life, are difficult. Therefore, we first use the DIC to observe the surface strain contour and the crack occurring. For example, Fig. 3(b) clearly shows some white spots which is corresponding to the initial crack propagation positions even some microcracking during the crack propagation. Combining the DIC images and the load-displacement curves, we determine the force P_0 at the crack initiation. For most of the samples, we found that the cracks start to propagate near the point of maximum load. Therefore, we determine that the initial cracking load P_0 is equal to the maximum load P_m. However, there may exist two different situations. When the original crack tip is in the hard material phase, the force P_0 at the crack initiation is equal to the maximum force P_m, such as at the point c3 of IPC-FCC (Fig. 3 (a)). While when the original crack tip is in the soft material phase, such as in the IPC-BCC, the crack will first propagate in the soft phase before reach the hard phase. This process causes a first max force P_{m1}, a stage and a second max force P_{m2}. Because our composites are non-homogeneous materials and for the fair comparison, we determine the force P_0 at the crack initiation is equal to the second maximum force P_{m2}. As expected, the IPCs achieve a higher fracture toughness than that of conventional PC, FC, LC composites. For example, the fracture toughness of FCC IPCs is about 16 times of that of FCC PCs. Therefore, combining additive manufacturing methods such as 3D printing technique, we provide a new insight to design periodic IPCs with complex 3D structures to achieve enhanced fracture behaviors.

3.2. Effect of material properties of compositions

3D printing technique not only enables the fabrication of complex structures in a timely and cheap manner but also allows for manufacturing composites with various combination of compositions. For example, IPCs with filled lattice structures including polyurethane/sand [53], metal/nano-particle liquid [54], and glassy polymer/rubber [55]

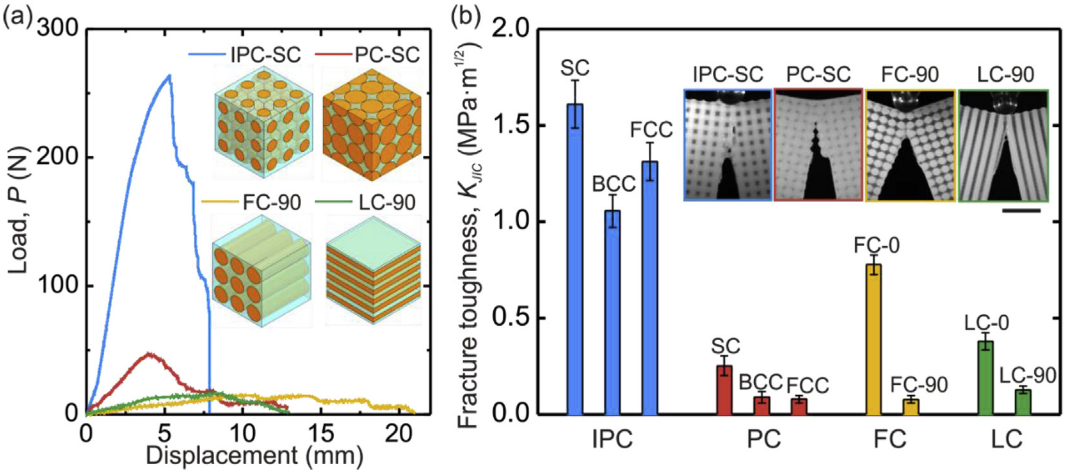

Fig. 5. 3-point bending tests of the SENB specimens of IPCs, PCs, FCs and LCs. (a) Load-displacement curves. (b) The calculated fracture toughness, K_J at zero crack extension of each IPC, PC, and LC. Images of specimens at failure strain showing the path of crack propagation for the SC IPC, SC PC, FC90, and LC90. Scale bar: 1 cm.

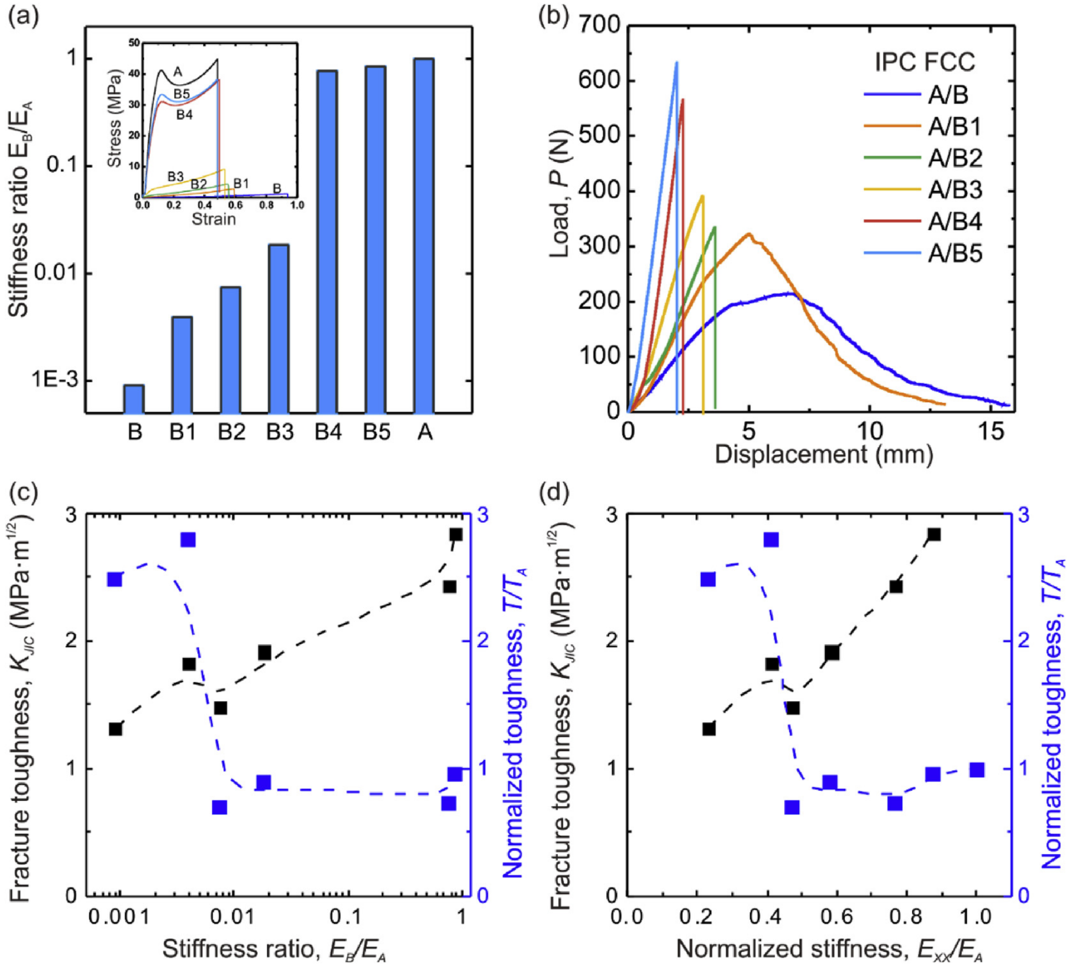

Fig. 6. The effect of stiffness ratio, E_B/E_A, on the mechanical response of FCC IPCs. (a) The calculated stiffness ratio of 3D printed constitutive materials from tension tests. (b) Load-displacement curves of IPC FCC SENB specimens with a variety of constituent materials. (c) Ashby plot indicating the correlation between calculated initial fracture toughness, K_{JIC}, normalized toughness T/T_A and the stiffness ratio, E_B/E_A. (d) Ashby plot indicating the correlation between calculated initial fracture toughness, K_{JIC}, normalized toughness T/T_A and the normalized stiffness ratio of each composite, E_{XX}/E_A. The dashed lines in (c) and (d) are guides to the eye. Here the volume fraction of material A is 50% for each composite.

all exhibit enhanced energy absorption ability. It has been also shown that the contrasts of the compositions have a significant impact on the mechanical response and fracture toughness [56–58]. Here the effect of stiffness ratio of two materials, E_B/E_A, on the evolution of fracture toughness is investigated. The material properties of the individual constituent materials are found by tensile testing of dogbone specimens comply with the ones prescribed by the ASTM D412 and ASTM D638. Fig. 6(a) presents the stress-strain relations of six different constitutive materials. It is clearly noted that material A, $B4$, and $B5$ behave relative stiff and brittle like glassy polymers while material B, $B1$, $B2$, and $B3$ are complaint ductile which are rubber-like polymers. The calculated tension modulus varies from around 1 MPa to 1 GPa, result in the stiffness ratios from 0.001 to 1 as shown in Fig. 6(a). However, material $B1-B5$ are constructed from a mix of material A and B and the mixing ratios are preprogrammed in the 3D printer and cannot be changed in the current setup. Therefore, the limited selection of materials available in Objet printing system constrains the value of stiffness ratio could not reach from 0.02 to 0.8. Fig. 6(b) displays the load-displacement response of SENB samples with a variety of constituent materials. The load-displacement curves indicate a wide variation of composite behavior as the constitutive behavior of the matrix (B) is tuned. It is clearly noticed that the composites transition in behavior from very stiff and brittle to a complaint ductile response. Moreover, the Ashby plots (Fig. 6(c)-(d)) show the relationship between the fracture toughness at crack initiation, K_{JIC}, the normalized toughness, T/T_A and the stiffness ratio, E_B/E_A, the normalized stiffness of composites E_{XX}/E_A, respectively. First, the fracture toughness at zero crack extension increases with increasing the stiffness ratio because the initial fracture toughness based on ASTM E1820 is largely affected by the maximum loading force during bending tests of SENB specimens and the stiffness of the composites. Therefore, the composites with stiffer and stronger matrix materials have larger fracture toughness at zero crack extension. Nonetheless, the displayed Ashby plots exhibit different trends for the normalized toughness which is a performance of engineered composites during the whole crack propagation process before catastrophic failure. It's shown that more compliant matrix phase is capable of creating tougher composites. This phenomenon is due to the fact that the weaker phase shifts the nature of load transfer in the composite to a more advantageous one [56]. Indeed, this mechanism has been observed in many biological materials [52]. These findings indicate that it is indeed possible to tune the interactions of the composite constituent phases through controlling the stiffness ratio to fundamentally alter the fracture mechanical properties of the composites.

3.3. Effect of volume fraction of each phase

It has been demonstrated the inherent architectures of IPC are of great importance to their fracture behavior [14,24,25]. Here, the effect of volume fraction on the evolution of fracture toughness is quantified (Fig. 7(a)). With the increase of volume fraction of the hard material,

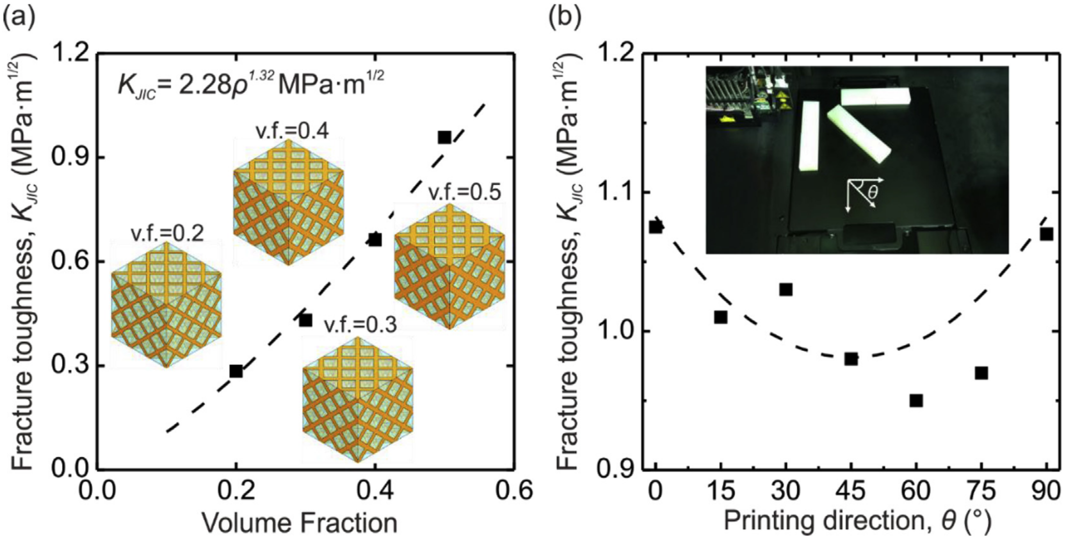

Fig. 7. The effect of the volume fraction of material *A* on the mechanical response of FCC IPCs. (a) The calculated fracture toughness, K_J at zero crack extension of the FCC IPC with different volume fractions. The effect of the 3D printing direction on the mechanical response of FCC IPCs. (b) The calculated fracture toughness, K_J at zero crack extension of IPCs. The inset schematically illustrates the printing direction. The dashed line is the fitting curve.

FCC IPCs exhibit a higher fracture toughness. This is because the load is mainly carried by the glassy polymer phase so that the composites with a higher content of material *A* show higher stiffness and strength. For cellular materials, such as metal foams and lattice structure, the relation between the effective elastic properties such as the elastic modulus E and the relative density $\bar{\rho}$ can be described by a power law $E \sim \bar{\rho}^n$ [59]. The scaling law is used to quantify the relation between the fracture toughness and the volume fraction of material *A* as $K_{JIC} = C\bar{\rho}^n$. For FCC IPCs, the scaling exponent n fitting from the experimental results equal to 1.32. This nearly linear scaling relation indicates that it's possible to design lightweight yet toughen composites. These results suggest good ability to tailor the geometric features of architected IPCs to achieve tunable mechanical properties and fracture toughness for purposeful mechanical applications.

3.4. Effect of 3D printing orientation

The effect of the 3D printing direction is also investigated on the mechanical response and fracture toughness of SENB samples as shown in Fig. 7(b). It can be seen that the direction of 3D-printing clearly influenced the fracture toughness. Note that the fracture toughness for composites printed in 0° and 90° directions are almost the same, whereas the weakest direction is depicted in 45° directions. This is because 3D printing induces anisotropy [60]. The 3D printed photopolymers exhibit that the elastic behavior, yield behavior, and plastic deformation all depend on the printing direction. Moreover, the material strength is highly anisotropic, which is usually much weaker along the printing direction. Considering the anisotropy effect inherited from the layer-wise processing feature, all the previous 3D printed samples except this group are fabricated along 0° directions. This finding suggests that fracture properties of IPC can be tailored by controlling the printing directions, thereby offering opportunities to design tough composites subjected to prescribed loading directions.

4. Conclusion

Through integrative rational design, 3D printing, and mechanical testing, we have quantitatively demonstrated that architected IPCs show improved fracture toughness compared with other conventional structured composites. Crack-bridging, process zone formation, and crack-deflection contribute to the enhanced fracture toughness, which are intrinsically controlled by the rationally designed interpenetrating architectures. A moderate increase in fracture resistance with crack growth is observed for the 3D printed IPCs. The proposed IPCs with the rod-connected counterparts and their inverse domains can be designed and tailored readily compared with other IPCs. Moreover, with the advance of 3D printing, the architected IPCs proposed here exhibit tunable fracture toughness, which enables the proposed architected IPC to confront complex loading conditions. Specifically, it's found that the interaction between a stiff and soft phase in an IPC could be tailored to create a tunable material system that exhibits significant stiffness combined with superior toughness. With the advance of additive manufacturing, it is possible to manufacture the proposed IPCs with different types of constitutive materials at various length scales, enabling us to further explore other material properties and functionalities, such as transport, thermal, phononic, and photonic to name a few. The findings presented here open avenues to explore advanced architected composites with multifunctionalities and tailorable properties through integrating rational architecture design and the state-of-the-art manufacturing techniques. Ongoing and future research addresses some approaches to simulate the mechanical properties especially the fracture behavior of these architected IPCs.

Acknowledgments

The authors gratefully acknowledge the support from the National Science Foundation (CMMI-1437449, CMMI-1462270), and the Office of Naval Research, United States (Dr. Yapa Rajapakse, Solid Mechanics Program).

Appendix A. Supplementary data

Supplementary data related to this article can be found at https://doi.org/10.1016/j.compscitech.2018.08.009.

References

[1] D.R. Clarke, Interpenetrating phase composites, J. Am. Ceram. Soc. 75 (4) (1992) 739–758.
[2] L. Wegner, L. Gibson, The mechanical behaviour of interpenetrating phase composites–I: modelling, Int. J. Mech. Sci. 42 (5) (2000) 925–942.
[3] L. Wegner, L. Gibson, The mechanical behaviour of interpenetrating phase composites–II: a case study of a three-dimensionally printed material, Int. J. Mech. Sci. 42 (5) (2000) 943–964.
[4] L. Wegner, L. Gibson, The mechanical behaviour of interpenetrating phase composites—III: resin-impregnated porous stainless steel, Int. J. Mech. Sci. 43 (4)

(2001) 1061–1072.

[5] Y.H. Ha, R.A. Vaia, W.F. Lynn, J.P. Costantino, J. Shin, A.B. Smith, P.T. Matsudaira, E.L. Thomas, Three-dimensional network photonic crystals via cyclic size reduction/infiltration of sea urchin exoskeleton, Adv. Mater. 16 (13) (2004) 1091–1094.

[6] E. Hamed, E. Novitskaya, J. Li, P.-Y. Chen, I. Jasiuk, J. McKittrick, Elastic moduli of untreated, demineralized and deproteinized cortical bone: validation of a theoretical model of bone as an interpenetrating composite material, Acta Biomater. 8 (3) (2012) 1080–1092.

[7] C.J. Hansen, W. Wu, K.S. Toohey, N.R. Sottos, S.R. White, J.A. Lewis, Self-healing materials with interpenetrating microvascular networks, Adv. Mater. 21 (41) (2009) 4143–4147.

[8] R. Jhaver, H. Tippur, Processing, compression response and finite element modeling of syntactic foam based interpenetrating phase composite (IPC), Mater. Sci. Eng., A 499 (1) (2009) 507–517.

[9] Z. Poniznik, V. Salit, M. Basista, D. Gross, Effective elastic properties of interpenetrating phase composites, Comput. Mater. Sci. 44 (2) (2008) 813–820.

[10] X.-Q. Feng, Y.-W. Mai, Q.-H. Qin, A micromechanical model for interpenetrating multiphase composites, Comput. Mater. Sci. 28 (3) (2003) 486–493.

[11] R.J. Moon, M. Tilbrook, M. Hoffman, A. Neubrand, Al–Al2O3 composites with interpenetrating network structures: composite modulus estimation, J. Am. Ceram. Soc. 88 (3) (2005) 666–674.

[12] C. Periasamy, H. Tippur, Experimental measurements and numerical modeling of dynamic compression response of an interpenetrating phase composite foam, Mech. Res. Commun. 43 (2012) 57–65.

[13] A. Agarwal, I. Singh, B. Mishra, Numerical prediction of elasto-plastic behaviour of interpenetrating phase composites by EFGM, Compos. B Eng. 51 (2013) 327–336.

[14] G. Li, X. Zhang, Q. Fan, L. Wang, H. Zhang, F. Wang, Y. Wang, Simulation of damage and failure processes of interpenetrating SiC/Al composites subjected to dynamic compressive loading, Acta Mater. 78 (2014) 190–202.

[15] D.W. Abueidda, A.S. Dalaq, R.K.A. Al-Rub, I. Jasiuk, Micromechanical finite element predictions of a reduced coefficient of thermal expansion for 3D periodic architectured interpenetrating phase composites, Compos. Struct. 133 (2015) 85–97.

[16] J.-H. Lee, L. Wang, S. Kooi, M.C. Boyce, E.L. Thomas, Enhanced energy dissipation in periodic epoxy nanoframes, Nano Lett. 10 (7) (2010) 2592–2597.

[17] J.-H. Lee, L. Wang, M.C. Boyce, E.L. Thomas, Periodic bicontinuous composites for high specific energy absorption, Nano Lett. 12 (8) (2012) 4392–4396.

[18] Y. Chen, L. Wang, Periodic co-continuous acoustic metamaterials with overlapping locally resonant and Bragg band gaps, Appl. Phys. Lett. 105 (19) (2014) 191907.

[19] Y. Liu, L. Wang, Enhanced stiffness, strength and energy absorption for co-continuous composites with liquid filler, Compos. Struct. 128 (2015) 274–283.

[20] H. Cho, J.C. Weaver, E. Pöselt, M.C. Boyce, G.C. Rutledge, Engineering the Mechanics of heterogeneous soft crystals, Adv. Funct. Mater. 26 (38) (2016) 6938–6949.

[21] L. Ai, X.-L. Gao, Evaluation of Effective Elastic Properties of 3D Printable Interpenetrating Phase Composites Using the Meshfree Radial Point Interpolation Method, Mech. Adv. Mater. Struct. (2016), https://doi.org/10.1080/15376494.2016.1143990.

[22] L.F. Wang, J. Lau, E.L. Thomas, M.C. Boyce, Co-continuous composite materials for stiffness, strength, and energy dissipation, Adv. Mater. 23 (13) (2011) 1524–1529.

[23] L.F. Wang, M.C. Boyce, C.Y. Wen, E.L. Thomas, Plastic dissipation mechanisms in periodic microframe-structured polymers, Adv. Funct. Mater. 19 (9) (2009) 1343–1350.

[24] T. Etter, J. Kuebler, T. Frey, P. Schulz, J. Löffler, P. Uggowitzer, Strength and fracture toughness of interpenetrating graphite/aluminium composites produced by the indirect squeeze casting process, Mater. Sci. Eng., A 386 (1) (2004) 61–67.

[25] M. Gao, Y. Pan, F. Oliveira, J. Baptista, J. Vieira, Interpenetrating microstructure and fracture mechanism of NiAl/TiC composites by pressureless melt infiltration, Mater. Lett. 58 (11) (2004) 1761–1765.

[26] L. Valdevit, A.J. Jacobsen, J.R. Greer, W.B. Carter, Protocols for the optimal design of multi-functional cellular structures: from hypersonics to micro-architected materials, J. Am. Ceram. Soc. 94 (s1) (2011) s15–s34.

[27] S. Shan, S.H. Kang, J.R. Raney, P. Wang, L. Fang, F. Candido, J.A. Lewis, K. Bertoldi, Multistable architected materials for trapping elastic strain energy, Adv. Mater. 27 (29) (2015) 4296–4301.

[28] B. Haghpanah, L. Salari-Sharif, P. Pourrajab, J. Hopkins, L. Valdevit, Multistable shape-reconfigurable architected materials, Adv. Mater. 28 (36) (2016) 7915–7920.

[29] T.A. Schaedler, W.B. Carter, Architected cellular materials, Annu. Rev. Mater. Res. 46 (2016) 187–210.

[30] G. Bullegas, S.T. Pinho, S. Pimenta, Engineering the translaminar fracture behaviour of thin-ply composites, Compos. Sci. Technol. 131 (2016) 110–122.

[31] M. Osanov, J.K. Guest, Topology optimization for architected materials design, Annu. Rev. Mater. Res. 46 (1) (2016) 211–233.

[32] O. Sigmund, Tailoring materials with prescribed elastic properties, Mech. Mater. 20 (4) (1995) 351–368.

[33] L.V. Gibiansky, O. Sigmund, Multiphase composites with extremal bulk modulus, J. Mech. Phys. Solid. 48 (3) (2000) 461–498.

[34] P. Vogiatzis, S. Chen, X. Wang, T. Li, L. Wang, Topology optimization of multi-material negative Poisson's ratio metamaterials using a reconciled level set method, Comput. Aided Des. 83 (2017) 15–32.

[35] E.C. Nelli Silva, J.S. Ono Fonseca, N. Kikuchi, Optimal design of periodic piezocomposites, Comput. Meth. Appl. Mech. Eng. 159 (1) (1998) 49–77.

[36] O. Sigmund, S. Torquato, Design of materials with extreme thermal expansion using a three-phase topology optimization method, J. Mech. Phys. Solid. 45 (6) (1997) 1037–1067.

[37] X. Wang, M. Jiang, Z. Zhou, J. Gou, D. Hui, 3D printing of polymer matrix composites: a review and prospective, Compos. B Eng. 110 (2017) 442–458.

[38] B.G. Compton, J.A. Lewis, 3D-printing of lightweight cellular composites, Adv. Mater. 26 (34) (2014) 5930–5935.

[39] L.S. Dimas, G.H. Bratzel, I. Eylon, M.J. Buehler, Tough composites inspired by mineralized natural materials: computation, 3D printing, and testing, Adv. Funct. Mater. 23 (36) (2013) 4629–4638.

[40] S. Hong, D. Sycks, H.F. Chan, S. Lin, G.P. Lopez, F. Guilak, K.W. Leong, X. Zhao, 3D printing of highly stretchable and tough hydrogels into complex, cellularized structures, Adv. Mater. 27 (27) (2015) 4035–4040.

[41] D.W. Abueidda, A.S. Dalaq, R.K.A. Al-Rub, H.A. Younes, Finite element predictions of effective multifunctional properties of interpenetrating phase composites with novel triply periodic solid shell architectured reinforcements, Int. J. Mech. Sci. 92 (2015) 80–89.

[42] G.X. Gu, M. Takaffoli, M.J. Buehler, Hierarchically enhanced impact resistance of bioinspired composites, Adv. Mater. 29 (28) (2017) 071006.

[43] D.W. Abueidda, A.S. Dalaq, R.K. Abu Al-Rub, H.A. Younes, Finite element predictions of effective multifunctional properties of interpenetrating phase composites with novel triply periodic solid shell architectured reinforcements, Int. J. Mech. Sci. 92 (2015) 80–89.

[44] O. Al-Ketan, R.K.A. Al-Rub, R. Rowshan, Mechanical properties of a new type of architected interpenetrating phase composite materials, Adv. Mater. Technol. 2 (2) (2017) 1600235.

[45] A.S. Dalaq, D.W. Abueidda, R.K.A. Al-Rub, Mechanical properties of 3D printed interpenetrating phase composites with novel architectured 3D solid-sheet reinforcements, Compos. Appl. Sci. Manuf. 84 (2016) 266–280.

[46] O. Al-Ketan, M. Adel Assad, R.K. Abu Al-Rub, Mechanical properties of periodic interpenetrating phase composites with novel architected microstructures, Compos. Struct. 176 (2017) 9–19.

[47] C. Bonatti, D. Mohr, Large deformation response of additively-manufactured FCC metamaterials: from octet truss lattices towards continuous shell mesostructures, Int. J. Plast. 92 (2017) 122–147.

[48] N.A. Fleck, R.A. Smith, Effect of density on tensile strength, fracture toughness, and fatigue crack propagation behaviour of sintered steel, Powder Metall. 24 (3) (1981) 121–125.

[49] L.D. Wegner, L.J. Gibson, The fracture toughness behaviour of interpenetrating phase composites, Int. J. Mech. Sci. 43 (8) (2001) 1771–1791.

[50] M.R. O'Masta, L. Dong, L. St-Pierre, H.N.G. Wadley, V.S. Deshpande, The fracture toughness of octet-truss lattices, J. Mech. Phys. Solid. 98 (2017) 271–289.

[51] D. Sen, M.J. Buehler, Structural hierarchies define toughness and defect-tolerance despite simple and mechanically inferior brittle building blocks, Sci. Rep. 1 (2011) 35.

[52] U.G.K. Wegst, H. Bai, E. Saiz, A.P. Tomsia, R.O. Ritchie, Bioinspired structural materials, Nat. Mater. 14 (1) (2015) 23–36.

[53] J. Zhou, X. Deng, Y. Yan, X. Chen, Y. Liu, Superelasticity and reversible energy absorption of polyurethane cellular structures with sand filler, Compos. Struct. 131 (2015) 966–974.

[54] Y. Liu, T.A. Schaedler, A.J. Jacobsen, W. Lu, Y. Qiao, X. Chen, Quasi-static crush behavior of hollow microtruss filled with NMF liquid, Compos. Struct. 115 (2014) 29–40.

[55] T. Li, Y. Chen, X. Hu, Y. Li, L. Wang, Exploiting negative Poisson's ratio to design 3D-printed composites with enhanced mechanical properties, Mater. Des. 142 (2018) 247–258.

[56] L.S. Dimas, M.J. Buehler, Modeling and additive manufacturing of bio-inspired composites with tunable fracture mechanical properties, Soft Matter 10 (25) (2014) 4436–4442.

[57] P. Murali, T.K. Bhandakkar, W.L. Cheah, M.H. Jhon, H. Gao, R. Ahluwalia, Role of modulus mismatch on crack propagation and toughness enhancement in bioinspired composites, Phys. Rev. 84 (1) (2011) 015102.

[58] P. Fratzl, H.S. Gupta, F.D. Fischer, O. Kolednik, Hindered crack propagation in materials with periodically varying Young's modulus—lessons from biological materials, Adv. Mater. 19 (18) (2007) 2657–2661.

[59] L.J. Gibson, M.F. Ashby, Cellular Solids: Structure and Properties, Cambridge university press, 1999.

[60] P. Zhang, A.C. To, Transversely isotropic hyperelastic-viscoplastic model for glassy polymers with application to additive manufactured photopolymers, Int. J. Plast. 80 (2016) 56–74.